actuators

MDPI

Article

Vehicle Attitude Control of Magnetorheological Semi-Active Suspension Based on Multi-Objective Intelligent Optimization Algorithm

Kailiang Han [1], Yiming Hu [1,2], Dequan Zeng [1], Yinquan Yu [1], Lei Xiao [1], Jinwen Yang [1], Weidong Liu [3,4] and Letian Gao [5,*]

[1] School of Mechatronics and Vehicle Engineering, East China Jiaotong University, Nanchang 330013, China; 20230380858000004@ecjtu.edu.cn (K.H.); huyiming139@hotmail.com (Y.H.); zdq1610849@126.com (D.Z.); yu_yinquan@ecjtu.edu.cn (Y.Y.); 20230380802000005@ecjtu.edu.cn (L.X.); 8652@ecjtu.edu.cn (J.Y.)
[2] Nanchang Automotive Institute of Intelligence & New Energy, Nanchang 330200, China
[3] School of Automotive Studies, Tongji University, Shanghai 201804, China; wliu18@jmc.com.cn
[4] Jiangling Motors Co., Ltd., Nanchang 330001, China
[5] Department of Civil and Environmental Engineering, UCLA, Los Angeles, CA 90095, USA
* Correspondence: letiangao@g.ucla.edu

Abstract: A multi-objective intelligent optimization algorithm-based attitude control strategy for magnetorheological semi-active suspension is proposed to address the vehicle attitude imbalance generated during steering and braking. Firstly, the mechanical properties of the magnetorheological damper (MRD) are tested, and the parameters in the hyperbolic tangent model of the magnetorheological damper are identified through experiments. Secondly, a simulation model of the whole vehicle multi-degree-of-freedom vehicle dynamics including magnetorheological damper is established, and the whole-vehicle Linear Quadratic Regulator (LQR) controller is designed. Then, the optimization design model of the joint vehicle controller and vehicle dynamics is established to design the optimization fitness function oriented to the body attitude control performance, and the attitude optimal controller is calculated with the help of multi-objective intelligent optimization algorithm. Simulation results show that the proposed control method is able to improve the body roll angle, body pitch angle, and suspension dynamic deflection well on the basis of ensuring no deterioration in other performance indexes, ensuring good attitude control capability of the vehicle and verifying the feasibility of the control strategy.

Keywords: magnetorheological damper; semi-active suspension; body attitude control; MOPSO-LQR control

check for updates

Citation: Han, K.; Hu, Y.; Zeng, D.; Yu, Y.; Xiao, L.; Yang, J.; Liu, W.; Gao, L. Vehicle Attitude Control of Magnetorheological Semi-Active Suspension Based on Multi-Objective Intelligent Optimization Algorithm. *Actuators* **2024**, *13*, 466. https://doi.org/10.3390/act13120466

Academic Editors: Michal Kubík and Janusz Gołdasz

Received: 14 October 2024
Revised: 16 November 2024
Accepted: 19 November 2024
Published: 21 November 2024

Copyright: © 2024 by the authors. Licensee MDPI, Basel, Switzerland. This article is an open access article distributed under the terms and conditions of the Creative Commons Attribution (CC BY) license (https://creativecommons.org/licenses/by/4.0/).

1. Introduction

As one of the most important components of a vehicle, the suspension system is responsible for supporting the body, damping vibrations, keeping the wheels in contact with the ground, and providing comfort and maneuverability. In the process of vehicle driving, the suspension system has a key role in improving the safety of vehicle driving and driver comfort [1]. As automotive technology has evolved, so have suspension systems.

Vehicle suspension systems can be classified into passive suspension, semi-active suspension, and active suspension based on the way the control force occurs, in which semi-active suspension has the advantages of low energy consumption, strong robustness, and high cost-effectiveness while improving vehicle stability and ride comfort [2,3]. Currently, there are two main types of actuators for semi-active suspensions: solenoid valve dampers and magnetorheological dampers [4]. Magnetorheological dampers are widely used in actuators, and some scholars have applied magnetorheological dampers to vehicle engine mounts and vehicle braking buffering processes [5,6], and the effects are remarkable. Meanwhile, magnetorheological dampers (MRDs) are simple and low-cost, with fast

response speed, low energy consumption, and adjustable direction of the output damping force during use, which can effectively improve the performance of the suspension in the application of semi-active suspensions, and have good research value [7,8]. By analyzing the damping characteristics of magnetorheological dampers, the establishment of an applicable and efficient magnetorheological damper model is the basis for magnetorheological dampers to give full play to their dynamic characteristics. For the establishment of mathematical models of magnetorheological dampers, many scholars have conducted research, and the mathematical models involved mainly include sigmoid model [9], neural network model [10], Bingham model, Bouc–Wen model [11], polynomial model [12], Jiles–Atherton model [13], and Hyperbolic tangent model, among others. The MRD hyperbolic tangent model uses the hyperbolic tangent function to describe the hysteresis properties [14], which can represent the rheological properties of magnetorheological fluids well and can be applied to different types of magnetorheological fluids as well as various application scenarios. In addition, the MRD hyperbolic tangent model is simple, has good flexibility and fitting accuracy in the process of MRD parameter identification, and also has high efficiency in computation, which has a wide range of applications in practice.

For the control of semi-active suspensions with magnetorheological dampers, a large part of the methods and theories of modern control theory can be applied to the control of semi-active suspensions, such as canopy control [15], robust control [16], fuzzy control [17], floor-shelter control, optimal control [18], and so on. Many scholars have fused the basic control methods to obtain, for example, adaptive fuzzy control [19], fuzzy sliding film PID control [20], smooth canopy control [21], and PID-LQR control [22]. In addition, some scholars have also integrated Kalman filtering [23] and intelligent optimization algorithm [24] into LQR control to obtain a more effective control method. However, the existing research on vehicle vertical motion control mainly focuses on the quarter suspension system, and there are relatively few studies on the whole vehicle attitude control involving semi-active suspension.

This paper establishes a seven-degree-of-freedom vehicle semi-active suspension model considering road excitation and longitudinal and lateral inertial acceleration, and obtains a hyperbolic tangent model of MRD, which can describe well the characteristics of MRD, through the experiments on the damping characteristics of MRD. The LQR control strategy is adopted to design the objective function with the main control objectives of body roll angle, body pitch angle, and suspension dynamic deflection characterizing the body attitude, and the multi-objective particle swarm algorithm is used for the controller design. Under the condition of ensuring that the remaining control variables will not change too much, the whole-vehicle LQR control strategy mainly focusing on body attitude control is designed and analyzed by numerical simulation. The body vertical acceleration, body pitch angle, body roll angle, suspension dynamic deflection, and tire dynamic deformation are used as the evaluation indexes. The obtained simulation results are compared with the uncontrolled passive suspension and traditional LQR semi-active suspension in the time and frequency domains to verify the effectiveness of the control strategy.

2. Damping Characteristic Test and Model of Magnetorheological Damper

The MRD hyperbolic tangent model utilizes the characteristics of the hyperbolic tangent function, which can describe well the characteristics of MRD. The relevant parameters in the hyperbolic tangent model can be obtained by experiments for parameter identification. The hyperbolic tangent model can be expressed as follows:

$$F = a_1 \tanh(a_2(v + k_0 s)) + a_3(v + k_0 x) - a_4, \quad (1)$$

where a_1 and k_0 are scaling factors, a_2 and a_3 are damping coefficients, a_4 is the offset damping force, and s and v are the expansion and contraction displacement and expansion speed of the damper, respectively.

Damping characteristics are tested using sinusoidal excitation, sinusoidal test peak speed is taken as 0.1 m/s, and the relationship between the parameter a1 and the current I under the action of different currents is shown in Figure 1.

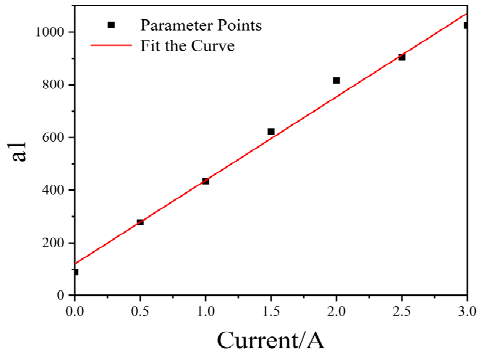


Figure 1. a1-I curve.

From Figure 1, it can be seen that the parameter a1 is a primary function of the current input I. Therefore, the hyperbolic tangent model can be rewritten as follows by $a_1 = aI + b$.

$$F = (aI + b)\tanh(a_2(v + k_0 s)) + a_3(v + k_0 x) - a_4, \quad (2)$$

A linear fit gives a = 317.4 and b = 119.8; I is the drive current input.

The output damping force–displacement curves under different currents are shown in Figure 2, and the output damping force–velocity curves are shown in Figure 3.

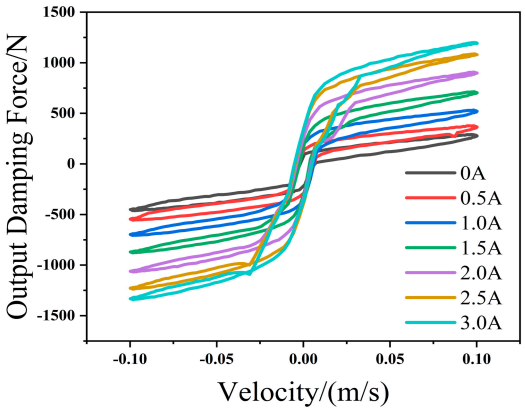


Figure 2. Damping force–displacement curve.

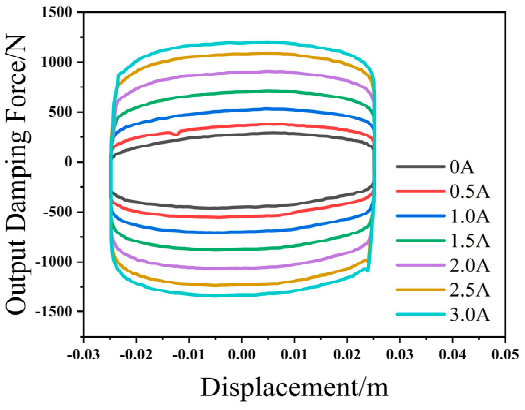


Figure 3. Damping force–velocity curve.

Based on the test data of the magnetorheological damper, the parameters of the hyperbolic tangent model of the magnetorheological damper can be determined by using genetic algorithm [25] for parameter identification, as shown in Table 1.

Table 1. Parameter identification results.

a_2	k_0	a_3	a_4	s
10.4223	0.8724	2357.3009	123.8307	39.51

The MRD hyperbolic tangent inverse model can be obtained from Equation (2) as follows:

$$I = \frac{\frac{F - a_3(v + k_0 x) + a_4}{\tanh(a_2(v + k_0 s))} - b}{a}, \tag{3}$$

3. Multi-Degree-of-Freedom Vehicle Model

In order to better characterize the body attitude, this paper establishes a multi-degree-of-freedom vehicle dynamics model including the body droop, pitch, and roll motions as well as the unsprung mass droop motion, as shown in Figure 4.

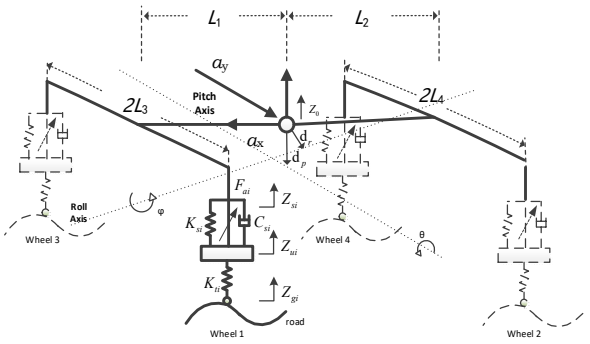


Figure 4. Multi-degree-of-freedom dynamics model.

According to Newton's second law, the equation of vibration at the center of mass of the sprung mass is given by the following equation:

$$m_s \ddot{z}_0 = \sum_{i=1}^{4} F_{si} \tag{4}$$

where m_s denotes the sprung mass, z_0 denotes the vertical displacement of the sprung mass, and i = 1, 2, 3, 4, denotes the left front wheel, left rear wheel, right front wheel, and right rear wheel. F_{si} denotes the total suspension force of the ith wheel, which is the sum of the damping, elastic, and actuating forces. F_{si} can be expressed as follows:

$$F_{si} = k_{si}(z_{ui} - z_{si}) + c_{si}(\dot{z}_{ui} - \dot{z}_{si}) + F_{ai} \tag{5}$$

where k_{si} and c_{si} represent the suspension stiffness and damping of the ith wheel, respectively, F_{ai} denotes the ideal damping force for the suspension of the ith wheel, and z_{ui} and z_{si} show the unsprung mass displacement and sprung mass displacement of the ith wheel.

The equations of motion for the rolling and pitching of the sprung mass under inertial acceleration are, respectively, as follows:

$$I_x \ddot{\phi} = (F_{s1} - F_{s3})L_3 + (F_{s2} - F_{s4})L_4 + m_s a_y d_r + m_s g d_r \phi \tag{6}$$

$$I_y \ddot{\theta} = (F_{s2} + F_{s4})L_2 - (F_{s1} + F_{s3})L_1 + m_s a_x d_p + m_s g d_p \theta \tag{7}$$

where I_x and I_y denote the lateral and pitch moment of inertia of the sprung mass, respectively; ϕ and θ denote the roll and pitch angles of the sprung mass, respectively; L_1 and L_2 denote the distances from the front axis to the center of mass and the distance from the rear axis to the center of mass; L_3 and L_4 denote the front half-axis wheelbase and the rear half-axis wheelbase; a_x and a_y denote the longitudinal and lateral inertial acceleration acting on the body; g is the acceleration of gravity; d_p and d_r denote the distance from the center of mass of the sprung mass to the pitch and roll axes.

The vibration equation for an unsprung mass is as follows:

$$m_{ui}\ddot{z}_{ui} = k_{ti}(z_{gi} - z_{ui}) - F_{si} \tag{8}$$

where m_{ui} denotes the unsprung mass of the ith wheel, k_{ti} is the tire stiffness of the ith wheel, and z_{gi} is the road input of the ith wheel.

When the roll angle and pitch angle are varied in a very small range, the displacements of the ith wheel's sprung mass are, respectively, as follows:

$$\begin{cases} z_1 = z_0 - L_1\theta + L_3\phi \\ z_2 = z_0 + L_2\theta + L_4\phi \\ z_3 = z_0 - L_1\theta - L_3\phi \\ z_4 = z_0 + L_2\theta - L_4\phi \end{cases} \tag{9}$$

Define $M_S = diag(m_s, I_x, I_y)$, $C_S = diag(c_{s1}, c_{s2}, c_{s3}, c_{s4})$, $K_S = diag(k_{s1}.k_{s2}, k_{s3}, k_{s4})$, $K_t = diag(k_{t1}.k_{t2}, k_{t3}, k_{t4})$, $Z_S = [z_0, \phi, \theta]^T$, $Z_U = [z_{u1}, z_{u2}, z_{u3}, z_{u4}]^T$, $Z_G = [z_{g1}, z_{g2}, z_{g3}, z_{g4}]^T$, $F_a = [F_{a1}, F_{a2}, F_{a3}, F_{a4}]^T$, $L = \begin{bmatrix} 1 & 1 & 1 & 1 \\ L_3 & L_4 & -L_3 & -L_4 \\ -L_1 & L_2 & -L_1 & L_2 \end{bmatrix}$, $L_{m1} = \begin{bmatrix} 0 & 0 \\ m_s d_r & 0 \\ 0 & m_s d_p \end{bmatrix}$, $L_{m2} = \begin{bmatrix} 0 & 0 & 0 \\ 0 & m_s g d_r & 0 \\ 0 & 0 & m_s g d_p \end{bmatrix}$.

With the above definitions, the vibration equations for the sprung mass, the lateral dip and pitch equations, and the vibration of the unsprung mass can be rewritten in the matrix form:

$$M_S\ddot{Z}_S = LK_S(Z_U - L^T Z_S) + LC_S(\dot{Z}_U - L^T\dot{Z}_S) + LF_a + L_{m1}Z_a + L_{m2}Z_S \tag{10}$$

$$M_U\ddot{Z}_U = K_t(Z_G - Z_U) - K_S(Z_U - L^T Z_S) - C_S(\dot{Z}_U - L^T\dot{Z}_S) - F_a \tag{11}$$

Selection of state variables: $X = \begin{bmatrix} Z_S \\ \dot{Z}_S \\ Z_U - L^T Z_S \\ Z_G - Z_U \\ \dot{Z}_U \end{bmatrix}$, output variables $Y = \begin{bmatrix} \ddot{Z}_S \\ Z_S \\ Z_U - L^T Z_S \\ Z_G - Z_U \end{bmatrix}$, control force input $U = F_a$, the system perturbation $W = Z_G$, expressed in the matrix form as a state equation of the form:

$$\begin{cases} \dot{X} = AX + BU + GW \\ Y = CX + DU + HW \end{cases} \tag{12}$$

where $A = \begin{bmatrix} 0_{3\times3} & 1_{3\times3} & 0_{3\times4} & 0_{3\times4} & 0_{3\times4} \\ M_S^{-1}L_{m2} & -M_S^{-1}LC_SL^T & M_S^{-1}LK_S & 0_{3\times4} & M_S^{-1}LC_S \\ 0_{4\times3} & -L^T & 0_{4\times4} & 0_{4\times4} & 1_{4\times4} \\ 0_{4\times3} & 0_{4\times3} & 0_{4\times4} & 0_{4\times4} & -1_{4\times4} \\ 0_{4\times3} & M_U^{-1}C_SL^T & -M_U^{-1}K_S & M_U^{-1}K_t & -M_U^{-1}C_S \end{bmatrix}_{18\times18}$, $B = \begin{bmatrix} 0_{3\times4} \\ M_S^{-1}L \\ 0_{4\times4} \\ 0_{4\times4} \\ -M_U^{-1} \end{bmatrix}_{18\times4}$,

$G = \begin{bmatrix} 0_{3\times2} & 0_{3\times4} \\ M_S^{-1}L_{m1} & 0_{3\times4} \\ 0_{4\times2} & 0_{4\times4} \\ 0_{4\times2} & 1_{4\times4} \\ 0_{4\times2} & 0_{4\times4} \end{bmatrix}_{18\times6}$, $C = \begin{bmatrix} M_S^{-1}L_{m2} & -M_S^{-1}LC_SL^T & M_S^{-1}LK_S & 0_{3\times4} & M_S^{-1}LC_S \\ 1_{3\times3} & 0_{3\times3} & 0_{3\times4} & 0_{3\times4} & 0_{3\times4} \\ 0_{4\times3} & 0_{4\times3} & 1_{4\times4} & 0_{4\times4} & 0_{4\times4} \\ 0_{4\times3} & 0_{4\times3} & 0_{4\times4} & 1_{4\times4} & 0_{4\times4} \end{bmatrix}_{14\times18}$,

$D = \begin{bmatrix} M_S^{-1}L \\ 0_{3\times4} \\ 0_{4\times4} \\ 0_{4\times4} \end{bmatrix}_{14\times4}$, $H = \begin{bmatrix} M_S^{-1}L_{m1} & 0_{3\times4} \\ 0_{3\times2} & 0_{3\times4} \\ 0_{4\times2} & 0_{4\times4} \\ 0_{4\times2} & 0_{4\times4} \end{bmatrix}_{14\times6}$.

MRD can only output the force in the same direction as the piston velocity because it has the output characteristics expressed in Equation (13). When the ideal damping force F_a is input to the inverse model of MRD, it is necessary to judge the direction of the control force and the piston's velocity, and it should be set to zero in order to avoid the opposite control effect when the control force is opposite to the piston's velocity.

$$F_{MRD} = \begin{cases} F_a & F_a \cdot (\dot{Z}_U - L^T\dot{Z}_S) \geq 0 \\ 0 & F_a \cdot (\dot{Z}_U - L^T\dot{Z}_S) < 0 \end{cases} \tag{13}$$

4. Design of Controller

The controller is divided into two parts, LQR controller is used in the bottom layer and multi-objective optimal matching layer is used in the top layer.

4.1. Design of the Underlying Controller

The optimal control of Linear Quadratic Regulator (LQR) is a classical multivariable control with state feedback to design the control law. The design objective of LQR controller is to balance the system performance and the control cost by minimizing the weight sum of the system's state quantities [26]. The LQR cost function is chosen as follows:

$$J = \int_0^\infty [Y^TQY + U^TRU]dt \tag{14}$$

where the input and output weight matrices are, respectively, as follows:

$$Q = diag(q_1, q_2, q_3, q_4 \ldots\ldots q_{14}) \tag{15}$$

$$R = diag(r_1, r_2, r_3, r_4) \tag{16}$$

In the weight matrix, q is the output weight coefficient, and r is the input weight coefficient. q and r reflect the relative importance of the output and input. The standard form of LQR control can be obtained by modifying the above equation:

$$J = \int_0^\infty \begin{bmatrix} X \\ U \end{bmatrix}^T \begin{bmatrix} E & N \\ N^T & F \end{bmatrix} \begin{bmatrix} X \\ U \end{bmatrix} dt \tag{17}$$

where $E = C^TQC$, $F = D^TQD + R$, $N = C^TQD$.

By solving the Riccati equation of the following form,

$$A^T P + PA - (PB + N)F^{-1}(B^T P + N^T) + E = 0, \tag{18}$$

the feedback gain matrix can be obtained

$$K = F^{-1}(B^T P + N^T); \tag{19}$$

then, the final control law is

$$U = -KX \tag{20}$$

4.2. Multi-Objective Particle Swarm Joint Optimization Design

The multi-objective parametric optimization problem of this paper is described as follows:

$$fitness(x) = \begin{cases} \{\min\{f_1(x), f_2(x), \cdots f_n(x)\}, x \in T, \exists K \\ \Omega, \exists K \end{cases} \tag{21}$$

where f(x) is the design objective function, n is the number of objective functions, T is the constraints, and Ω is the penalty function.

4.2.1. Design Objectives

In this study, the body roll angle, body pitch angle, and suspension dynamic deflection, which characterize the body attitude, are mainly taken as the main control objectives, so that the body attitude can be well controlled under the circumstance of ensuring that the rest of the control variables will not change too much. Therefore, the designed objective function is selected as follows:

(1) Selection of body roll angle, body pitch angle, and suspension dynamic deflection characterizing the control of the body attitude.

$$f_1(x) = \frac{RMS(\phi)}{RMS_P(\phi)} + \frac{RMS(\theta)}{RMS_P(\theta)} + \frac{RMS(Z_U - L^T Z_S)}{RMS_P(Z_U - L^T Z_S)} \tag{22}$$

where $RMS(\phi)$, $RMS(\theta)$, and $RMS(Z_U - L^T Z_S)$ are the root mean square values of the semi-active suspension body roll angle, pitch angle, and suspension dynamic deflection, and $RMS_P(\phi)$, $RMS_P(\theta)$, and $RMS_P(Z_U - L^T Z_S)$ are the root mean square values of the passive suspension body roll angle, pitch angle, and suspension dynamic deflection.

(2) Selection of body vertical acceleration, body roll acceleration, and body pitch acceleration to characterize ride smoothness.

$$f_2(x) = \frac{RMS(\ddot{Z}_S)}{RMS_P(\ddot{Z}_S)} + \frac{RMS(\ddot{\phi})}{RMS_P(\ddot{\phi})} + \frac{RMS(\ddot{\theta})}{RMS_P(\ddot{\theta})} \tag{23}$$

where $RMS(\ddot{Z}_S)$, $RMS(\ddot{\phi})$, and $RMS(\ddot{\theta})$ are the root mean square values of the semi-active suspension body vertical acceleration, body roll acceleration, and body pitch acceleration, and $RMS_P(\phi)$, $RMS_P(\theta)$, and $RMS_P(Z_U - L^T Z_S)$ are the root mean square values of the passive suspension body vertical acceleration, body roll acceleration, and body pitch acceleration.

(3) Selection of tire dynamic deformation to characterize handling stability

$$f_3(x) = \frac{RMS(Z_G - Z_U)}{RMS_P(Z_G - Z_U)} \tag{24}$$

where $RMS(Z_G - Z_U)$ is the root mean square value of the semi-active suspension tire dynamic deformation, and $RMS_P(Z_G - Z_U)$ is the root mean square value passive suspension tire dynamic deformation.

(4) Establishment of comprehensive evaluation indicators through the above three objective functions:

$$f_4(x) = \alpha_1 f_1(x) + \alpha_2 f_2(x) + \alpha_3 f_3(x) \tag{25}$$

α is the weighting factor, taking $\alpha_1 = 0.5$, $\alpha_2 = 0.25$, and $\alpha_3 = 0.25$, making the overall control effect tilted towards the body attitude.

4.2.2. Variable and Penalty Function Design

The design variables are

$$x = [q_1, q_2, \cdots q_{14}, r_1, \cdots, r_4] \tag{26}$$

Based on the symmetry of the dynamics model, there are $q_7 = q_8 = q_9 = q_{10}$, $q_{11} = q_{12} = q_{13} = q_{14}$, $r_1 = r_2 = r_3 = r_4$.

According to the characteristics of the LQR optimal controller, if the Hamiltonian matrix of the system does not have an eigenroot on the imaginary axis of the complex coordinate system, then the controller will not be able to compute the gain matrix K, and the optimal design process will be erroneous and interrupted. In order to avoid this and keep the population away from erroneous solutions, it is necessary to design a penalty function that is consistent with the dimensionality of the objective space.

$$\Omega = \{\delta, \delta, \cdots, \delta\}_{1\times n} \tag{27}$$

where δ is the larger positive number.

If the gain matrix K cannot be calculated, then the value of the fitness function fitness(x) will not be available. At this point, a larger value can be assigned to fitness(x) as a solution. The optimization algorithm will automatically exclude this poorer solution and steer the population away from this solution to avoid interruption of the iterative process.

4.2.3. Optimizing the Design Process

The design objective dimension $n = 4$ and design variable dimension $m = 9$ are summed up in this study.

The optimal design flow of multi-objective particle swarm algorithm is shown in Figure 5.

4.2.4. Multi-Objective Particle Swarm Algorithm Parameter Selection

The selection of the parameters of the particle swarm algorithm has a great impact on the results of the optimization design. The population size and the number of iteration steps are two key parameters, which together determine the length of the iteration time and the accuracy of the calculation results. In this study, according to the specific calculation conditions, the population size of 500 is selected, the maximum iteration step is 1000 steps, and the upper limit of the external set is set to $l_{max} = 500$.

Inertia weights Wf are used to balance global and local search. A larger Wf usually has stronger global search capability, while a smaller Wf is better at local search. In this study, the inertia weight Wf is used to change linearly with the iteration steps, with Wf of 0.7 at the beginning and 0.4 at the end, so that the algorithm has a strong global search capability at the beginning of the iteration and enhances its local search capability at the end of the iteration.

The weighting factors R_1 and R_2 are used to characterize how much weight the particle population gives to individual experience versus global experience in the search direction selection process. They are usually set as standard weights, i.e., $R_1 = R_2 = 2$, implying that individual experience is given the same weight as global experience in the decision-making process.

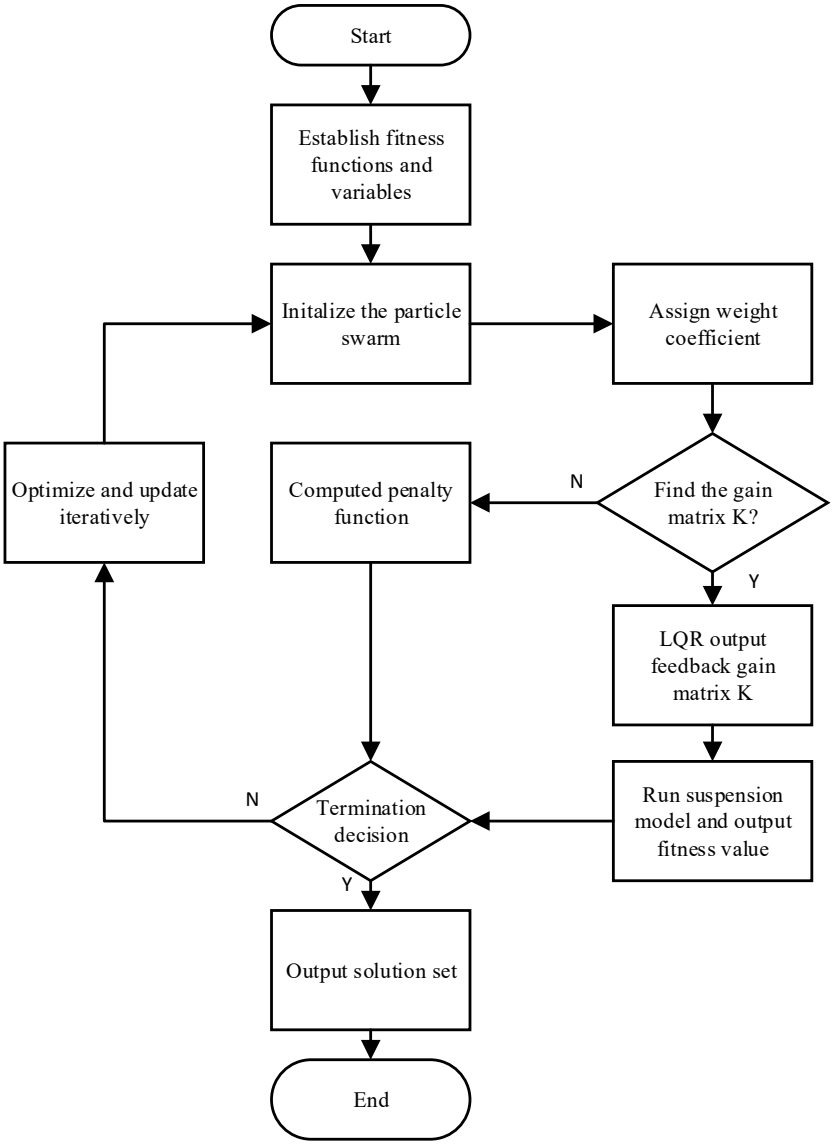


Figure 5. Flowchart of multi-objective particle swarm algorithm.

The penalty coefficient δ takes a large positive number; in principle, the penalty coefficient δ needs to be much larger than the value of the objective function, and in this study, $\delta = 1 \times 10^9$.

5. Comparative Simulation Analysis

In order to verify the effectiveness of the design strategy, the passive suspension and semi-active suspension are analyzed by numerical simulation using random road excitation. The stochastic pavement excitation adopts the filtered white noise time domain pavement input model [27], which is as follows:

$$\dot{q}(t) = -2\pi f_0 q(t) + 2\pi\sqrt{S_q(n_0)uw}(t) \tag{28}$$

where is the lower cut-off frequency of f_0, u is the vehicle traveling speed, w(t) is the uniformly distributed white noise, and $S_q(n_0)$ is the pavement unevenness coefficient. In this study, we use class C pavement as the random pavement input, the unevenness coefficient of class C pavement is $S_q(n_0) = 0.000256$, and the lower cut-off frequency is taken as $f_0 = 0.07$.

5.1. Vehicle Simulation Parameter Selection

The parameters of the whole vehicle used for simulation are shown in Table 2.

Table 2. Vehicle parameters.

Parameters	Value	Unit
Sprung mass	1400	kg
Pitch inertia	2100	$kg \cdot m^2$
Roll inertia	450	$kg \cdot m^2$
Front suspension stiffness	21,500	N/m
Rear Suspension stiffness	22,500	N/m
Front suspension damping	1700	$N/(m \cdot s^{-1})$
Rear suspension damping	1700	$N/(m \cdot s^{-1})$
Unsprung mass at front wheels	40.5	kg
Unsprung mass at rear wheels	45.4	kg
Front tire stiffness	180,360	N/m
Rear tire stiffness	170,360	N/m
Centroid to front axle distance	1.4	m
Centroid to front axle distance	1.7	m
Front half shaft distance	0.75	m
Rear half shaft distance	0.75	m

In the simulation, the longitudinal inertial acceleration of the vehicle is taken as $a_x = -6\ m/s^2$, the lateral inertial acceleration is taken as $a_y = 4\ m/s^2$, and the initial velocity $v_0 = 15\ m/s$.

5.2. Pareto Typical Solution Selection

By selecting the fitness values of different objective functions as the x, y, and z axes, the objective Pareto front view can be obtained as shown in Figure 6. The solutions in the Pareto optimal solution set satisfy the non-dominated relationship with each other.

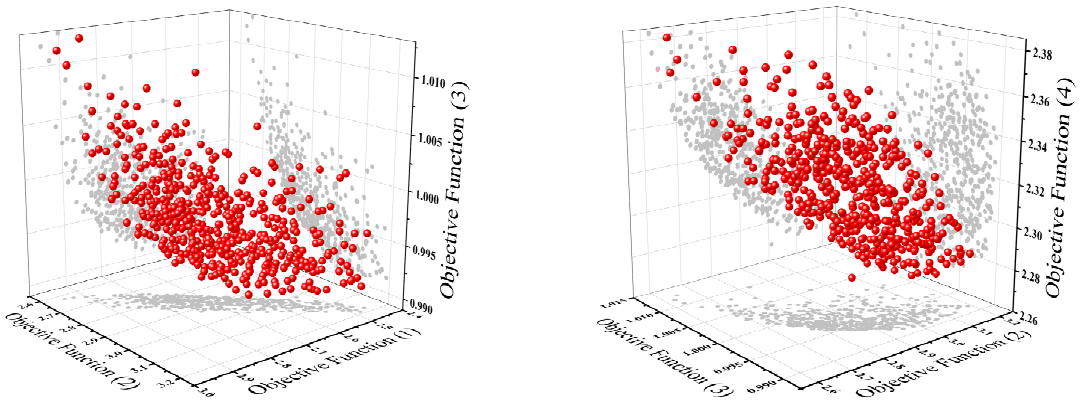


Figure 6. Pareto front viewable view.

Pareto solution is a set of non-dominated solutions; in order to select representative solutions from these solutions as the required weight coefficients, this paper adopts the fuzzy set theory for the preference to eliminate the influence of human factors on the selection of the optimal solution [28]. The affiliation function is defined as follows:

$$S_i^j = \begin{cases} 0, & f_i^j \geq f_i^{\max} \\ \dfrac{f_i^{\max} - f_i}{f_i^{\max} - f_i^{\min}}, & f_i^{min} < f_i^j < f_i^{\max} \\ 1, & f_i^j \leq f_i^{\min} \end{cases} \tag{29}$$

where S_i^j and f_i^j are the affiliation value and current value of the ith optimization objective of the jth solution; f_i^{min} and f_i^{max} are the minimum and maximum value of the ith optimization objective in the solution set.

The dominant function is defined as follows:

$$\varphi_k = \sum_{i=1}^{n} S_i^k / (\sum_{j=1}^{l} \sum_{i=1}^{n} S_i^j) \tag{30}$$

where n is the number of objective functions; in this study, $n = 4$; l is the number of solutions in the external set.

According to the above equation, the dominance values of all solutions in the external set are calculated, and the solution with the largest dominance value is selected as the typical solution of the Pareto optimal solution set, as shown in Figure 7.

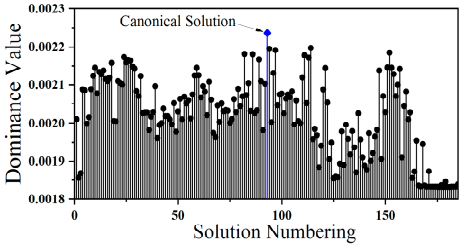


Figure 7. Dominance value of each solution.

5.3. Damping Force Analysis

Magnetorheological damping has a millisecond response speed, far exceeding that of conventional damping-controlled dampers. Magnetorheological dampers can adjust the magnitude of the damping force by the magnitude of the current, thus achieving continuously adjustable damping. The actual damping force F_{MRD} output from the magnetorheological damper and the ideal damping force F_a obtained from the controller calculation are shown in Figure 8.

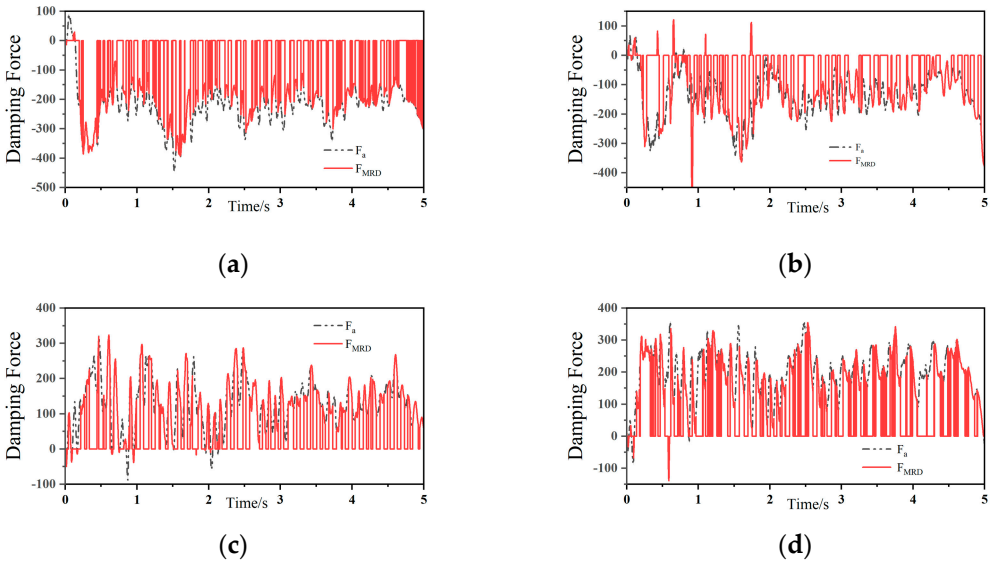


Figure 8. Damping force comparison: (**a**) damping force of the left front tire; (**b**) damping force of the left rear tire; (**c**) damping force of the right front tire; and (**d**) damping force of the right rear tire.

As shown in Figure 8, the hyperbolic tangent model of the magnetorheological damper can generate the damping force well according to the input current, and the generated damping force is very close to the ideal damping force calculated by the controller. This

study focused on the attitude control of the car body and considers both lateral and longitudinal inputs when building the dynamics model, so the ideal damping force will be biased in a certain direction, and the actual damping force obtained in the end shows similar characteristics.

5.4. Time Domain Response Analysis

Table 3 shows the comparison of the root mean square plant for each evaluation metric.

Table 3. Root mean square plant for each evaluation metric.

	Passive Suspension	LQR Semi-Active Suspension	MOPSO-LQR Semi-Active Suspension	Relative Rate of Change/%	
				Passive Suspension	LQR Semi-Active Suspension
Body roll angle	2.0258	1.844	1.6832	16.92	8.72
Body pitch angle	0.3852	0.3570	0.3198	17.65	10.42
Body vertical acceleration	0.2914	0.2793	0.3012	−3.37	−7.84
Body roll angle acceleration	0.7037	0.6855	0.6578	6.53	3.96
Body pitch angle acceleration	0.2562	0.277	0.2657	−3.71	4.07
Left front suspension deflection	0.0300	0.0269	0.0248	17.42	7.8
Left rear suspension deflection	0.0169	0.0169	0.0134	20.93	20.93
Right front suspension deflection	0.0172	0.0159	0.0139	19.25	12.5
Right rear suspension deflection	0.0296	0.0249	0.0245	17.37	1.6
Left front tire dynamic deformation	0.0039	0.0039	0.0038	2.56	2.56
Left rear tire dynamic deformation	0.0027	0.0028	0.0027	0	3.5
Right front tire dynamic deformation	0.0026	0.0027	0.0027	−2.64	0

Figure 9 shows that the time domain response curves characterize the body attitude control quantities such as body roll angle, body pitch angle, and suspension dynamic deflection. Table 3 shows the comparison of the root mean square plant for each evaluation metric.

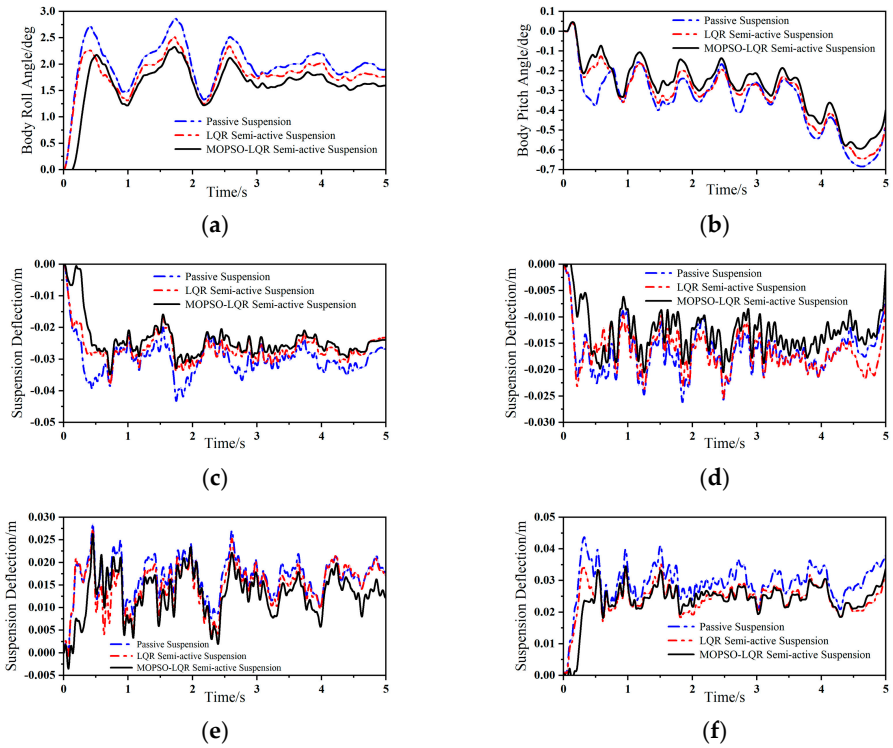


Figure 9. Time domain response curve of body attitude: (**a**) body roll angle; (**b**) body pitch angle; (**c**) left front suspension deflection; (**d**) left rear suspension deflection; (**e**) right front suspension deflection; and (**f**) right rear suspension deflection.

As shown in Figure 9, the MOPSO-LQR controlled semi-active suspension is relieved in body pitch angle, body roll angle, and suspension dynamic deflection. Combined with the comparison of the root mean square values in Table 3, it can be seen that the root mean square plant MOPSO-LQR semi-active suspension reduces the body lean angle and body pitch angle by 16.92% and 7.31% compared to the passive suspension, and the suspension dynamic deflection is reduced by 18.74% on average for all four wheels. Compared with the LQR semi-active suspension, the MOPSO-LQR semi-active suspension reduces the body roll and pitch angles by 8.72% and 10.42% and reduces the suspension dynamic deflection by an average of 10.71% in all four wheels, which achieves a good control of the body attitude.

Figure 10 shows the time domain response curves of body vertical acceleration and tire dynamic deformation.

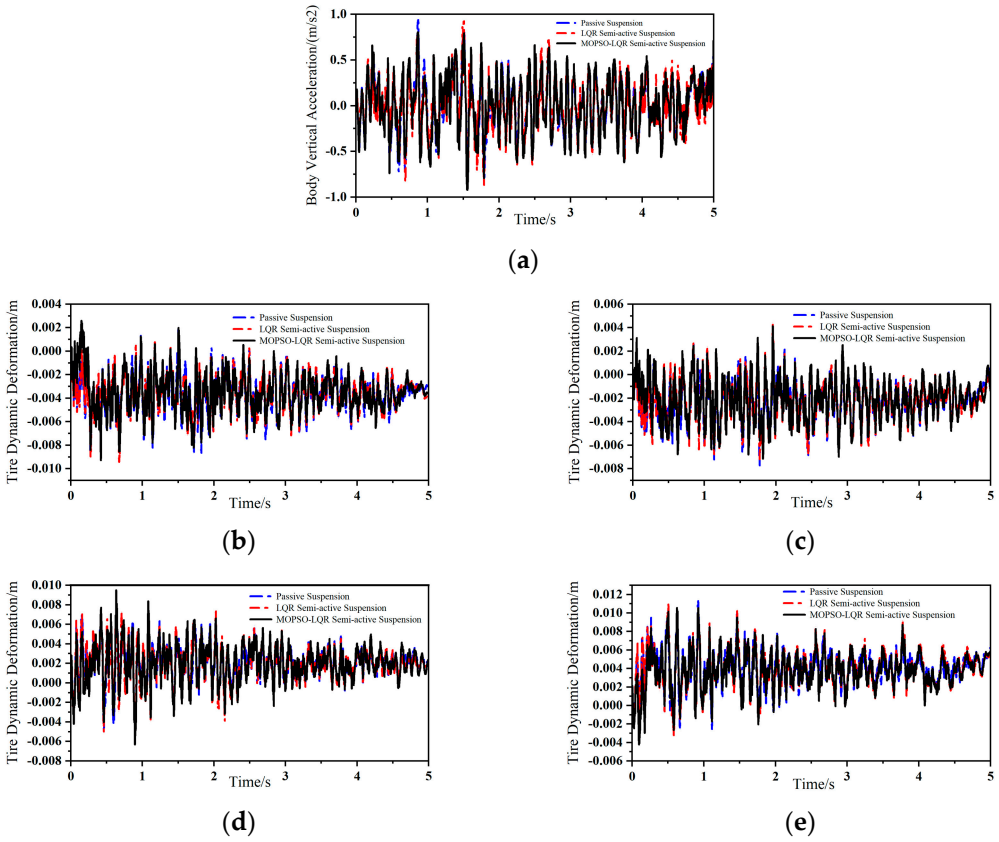


Figure 10. Time domain response curves of vertical acceleration and tire dynamic deformation: (**a**) body vertical acceleration; (**b**) dynamic deformation of the left front tire; (**c**) dynamic deformation of the left rear tire; (**d**) dynamic deformation of the right front tire; and (**e**) dynamic deformation of the right rear tire.

As can be seen from Figure 10, the body vertical acceleration and four-wheel tire dynamic deformation did not change significantly, when combined with the root mean square plant comparisons in Table 3. Compared to passive suspension, MOPSO-LQR semi-active suspension body vertical acceleration worsened by 3.37%, and for the four-wheel tire dynamic deformation, the right front tire worsened by 2.64%, while the left front tire and right rear tire improved by 2.56% and 2.33%, respectively. In addition, the body pitch angle acceleration worsened by 3.71% and the body roll angle acceleration improved. Compared to the LQR semi-active suspension, the MOPSO-LQR semi-active suspension has a more severe deterioration in body droop acceleration but has improvements in three areas: body roll acceleration, body pitch acceleration, and tire dynamic deformation.

The results show that although some indicators have deteriorated, the deterioration is within acceptable limits.

5.5. Frequency Domain Response Analysis

The time domain analysis is only for specific pavement conditions and does not reflect the response under other conditions, so the system needs to be analyzed in the frequency domain. The exogenous excitation is taken as a new input to the system, and the obtained control law is substituted into the state equation of the system to obtain the following:

$$\begin{cases} \dot{X} = (A - BK)X + GW \\ Y = (C - DK)X + HW \end{cases} \tag{31}$$

The input–output correspondences of interest therein are listed in Table 4.

Table 4. Correspondence between key inputs and outputs.

	Body Vertical Acceleration	Body Roll Angle	Body Pitch Angle	Suspension Deflection	Tire Dynamic Deformation
Lateral accelerations		√		√	√
Longitudinal acceleration			√	√	√
Road input	√			√	√

The frequency domain response curve of the road input to a typical output is shown in Figure 11.

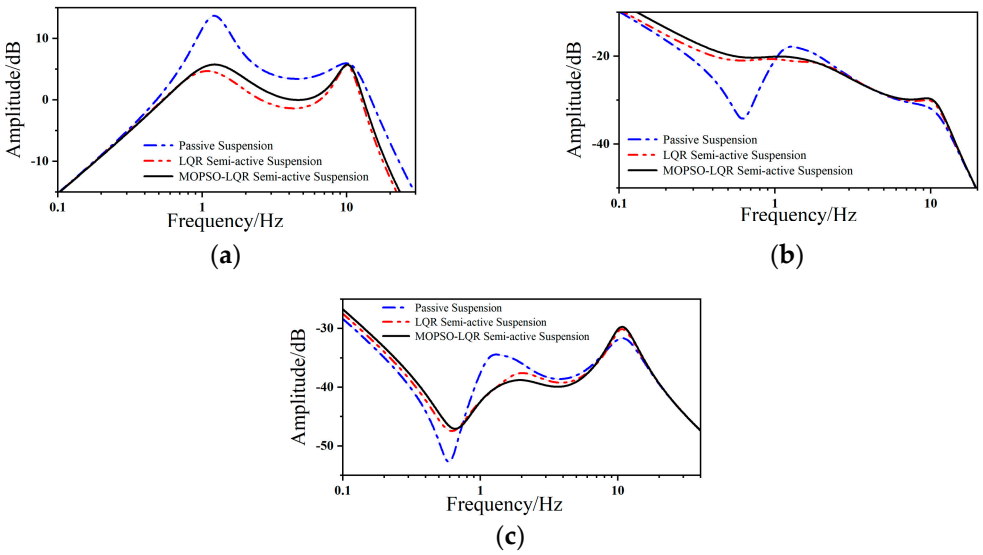


Figure 11. Frequency domain curve of road input against typical output: (**a**) road input to body vertical acceleration; (**b**) road input to suspension dynamic deflection; and (**c**) road input to tire dynamic deformation.

As can be seen from Figure 11, for the MOPSO-LQR semi-active suspension, the body vertical acceleration response due to road excitation is reduced, and the suspension deflection response and tire dynamic deformation response are improved in the low-frequency band, but the responses are still in the reasonable range. In the range of 1–10 Hz, the suspension deflection response and tire dynamic deformation response are lower than the response of the passive suspension and LQR semi-active suspension, and the performance is improved.

The frequency domain response curve of lateral acceleration to a typical output is shown in Figure 12.

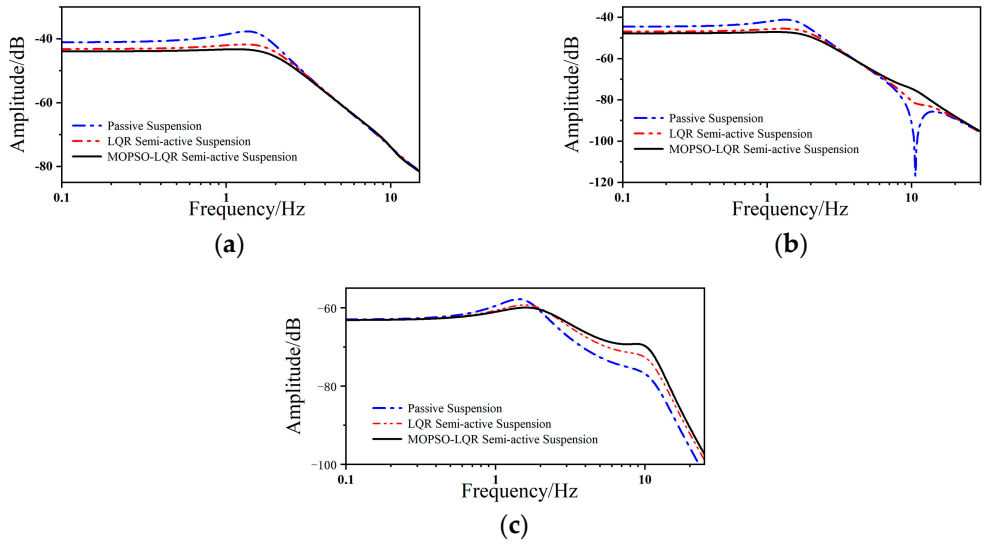


Figure 12. Frequency domain curve of lateral acceleration against typical outputs: (**a**) lateral acceleration to body roll angle; (**b**) lateral acceleration to suspension dynamic deflection; and (**c**) lateral acceleration to tire dynamic deformation.

Steering operations tend to be low-frequency operations, so the results of interest for the response due to inertial acceleration induced under steering conditions are dominated by the low-frequency band response. Comparing the body roll angle, suspension deflection, and tire dynamic deformation due to lateral inertial acceleration, the response of MOPSO-LQR semi-active suspension is better than the passive suspension response and the LQR semi-active suspension in the low-frequency band. In addition, it is obvious from Figure 12b that there is a trapping effect on the dynamic deflection response of the suspension at 10 Hz for the passive suspension. If such an operation exists, there is no suspension deformation at this point, allowing energy to be transferred to the body, which can easily cause a rollover to occur, and the MOPSO-LQR semi-active suspension improves this phenomenon more than the LQR semi-active suspension.

The frequency domain response curve of longitudinal acceleration to a typical output is shown in Figure 13.

The operation under braking conditions is similar to that under steering conditions, and the response due to longitudinal inertial acceleration is mainly in the low-frequency band. As can be obtained from Figure 13, the body pitch angle, suspension deflection, and tire runout under the influence of longitudinal inertial acceleration, the response of MOPSO-LQR semi-active suspension is better than the response of passive suspension and LQR semi-active suspension at the low-frequency band. Figure 13b shows that, under braking conditions, the passive suspension also has a trapping effect on the suspension dynamic deflection response at 10 Hz, while the MOPSO-LQR semi-active suspension does not exhibit this phenomenon, and the improvement is higher than that of the LQR semi-active suspension.

In summary, in terms of frequency domain response, compared with the passive suspension and LQR semi-active suspension, the MOPSO-LQR semi-active suspension system can achieve multi-objective balance, which can significantly improve the response of body roll, pitch, and suspension dynamic deflection, especially in the low-frequency band, and demonstrates a very good body attitude control effect.

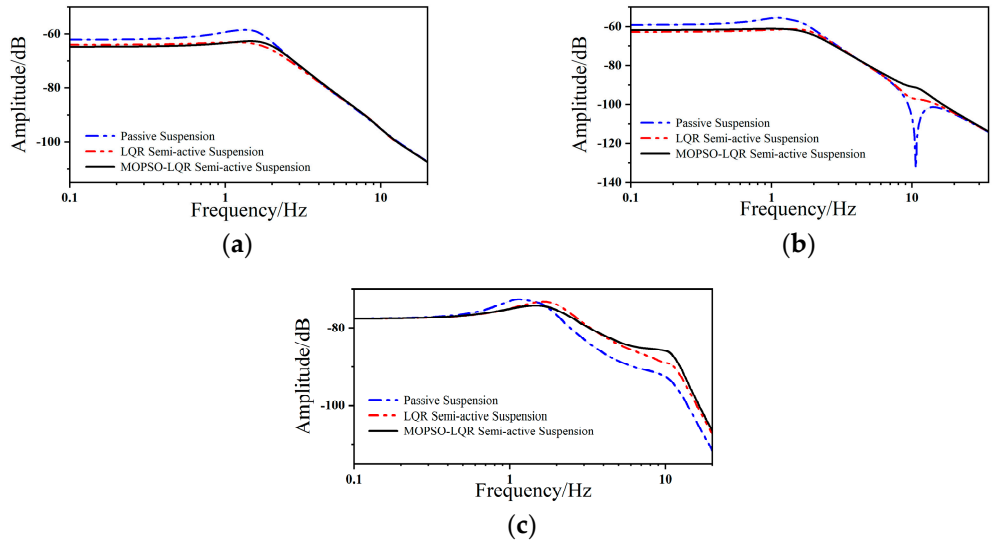


Figure 13. Frequency domain curves of longitudinal acceleration against typical outputs: (**a**) longitudinal acceleration to body pitch angle; (**b**) longitudinal acceleration to suspension deflection; and (**c**) longitudinal acceleration to tire dynamic deformation.

6. Conclusions

Based on the vehicle dynamics model with multiple degrees of freedom considering the vehicle attitude such as pitch and roll, this study assesses the vehicle attitude control under the compound condition of steering and braking, and designs the vehicle magnetorheological semi-active suspension controller guided by the vehicle attitude control.

(1) Experiments on the mechanical properties of the magnetorheological damper were carried out to obtain a hyperbolic tangent model describing the properties of the magnetorheological damper.

(2) Based on the multi-degree-of-freedom vehicle dynamics simulation model, a joint optimization design model of vehicle LQR controller and vehicle dynamics was established. The body attitude as the main control objective was designed to optimize the fitness function, and the attitude optimal controller was obtained by multi-objective intelligent optimization algorithm.

(3) Simulink co-simulation results show that, when considering the braking and steering conditions, in the time domain, the MOPSO-LQR semi-active suspension reduces the mean square roots of body roll and pitch angle by 16.92% and 17.65%, respectively, and the four-wheel average of suspension dynamic deflection by 18.74% compared to the passive suspension. Compared with the LQR semi-active suspension, the mean square roots of body roll and pitch angle are reduced by 8.72% and 10.42%, respectively, and the suspension dynamic deflection is reduced by 10.71% on average for all four wheels. In the frequency domain characteristics, the body roll angle response, body pitch angle response, and suspension dynamic deflection response caused by the external excitation of the semi-active suspension are overall better than the passive suspension and LQR semi-active suspension, optimizing the body attitude frequency response. On the other hand, the global optimum of comfort and attitude stability is achieved in general, although some metrics deteriorate within the time and frequency domains.

Author Contributions: Conceptualization, K.H.; methodology, K.H., Y.H. and D.Z.; resources, Y.H. and D.Z.; data curation, L.X.; writing—original draft preparation, K.H.; writing—review and editing, Y.Y. and K.H.; supervision, W.L. and L.G.; project administration, J.Y. All authors have read and agreed to the published version of the manuscript.

Funding: This paper was supported by The National Natural Science Foundation of China (Grant No. 52302470; Grant No. 52462053), The Ganpo Talent Support Program-Leading Academic and Technical Personnel in Major Disciplines of Jiangxi Province (Grant No. 20232BCJ23091); The Natural Science Foundation of Jiangxi Province (Grant No. 20232BAB214092; Grant No. 20224BAB214045), The Key R&D Program of Jiangxi Province (Grant No. 20224BBE51048; Grant No. 20232BBE50009; Grant No. 20232BBE50010); The 03 Special Program and 5G Project of Jiangxi Province (Grant No. 20232ABC03A30); and The Open Bidding for Selecting the Best Candidates Program of Nanchang (Grant No. 2022JBGS001).

Data Availability Statement: The data supporting this study's findings are available from the corresponding authors upon reasonable request.

Acknowledgments: The authors thank the participants, institutions, editors, and reviewers for enabling us to conduct this research.

Conflicts of Interest: Author Weidong Liu was employed by Jiangling Motors Co., Ltd. The authors declare no conflicts of interest.

References

1. Lu, H.; Zhang, Z.; Xu, Z.; Tan, K.; Zheng, X. Equivalence of Sub-optimal control strategy for vehicle active suspension. *Vib. Shock* **2023**, *42*, 316–324.
2. Gong, M.; Wang, H.; Wang, X. Active Suspension Control Based on Estimated Road Class for Off-Road Vehicle. *Math. Probl. Eng.* **2019**, *2019*, 3483710. [CrossRef]
3. Wu, J.; Zhou, H.; Liu, Z.; Gu, M. Ride comfort optimization via speed planning and preview semi-active suspension control for autonomous vehicles on uneven roads. *IEEE Trans. Veh. Technol.* **2020**, *69*, 8343–8355. [CrossRef]
4. Peng, Z.; Wei, Y.; Fu, X.; Yao, X. Research and Performance Test of Magnetorheological Semi-Active Suspension System Based on a Real Vehicle. *Automot. Eng.* **2021**, *43*, 269–277. [CrossRef]
5. Choi, S.B.; Song, H.J.; Lee, H.H.; Lim, S.C.; Kim, J.H.; Choi, H.J. Vibration control of a passenger vehicle featuring magnetorheological engine mounts. *Int. J. Veh. Des.* **2003**, *33*, 2–16. [CrossRef]
6. Milecki, A.; Sedziak, D.; Ortmann, J.; Hauke, M. Controllability of MR shock absorber for vehicles. *Int. J. Veh. Des.* **2005**, *38*, 222–233. [CrossRef]
7. Yıldız, A.S.; Sivrioğlu, S.; Zergeroğlu, E.; Çetin, Ş. Nonlinear adaptive control of semi-active MR damper suspension with uncertainties in model parameters. *Nonlinear Dyn.* **2015**, *79*, 2753–2766. [CrossRef]
8. Hemanth, K.; Kumar, H.; Gangadharan, K. Vertical dynamic analysis of a quarter car suspension system with MR damper. *J. Braz. Soc. Mech. Sci. Eng.* **2017**, *39*, 41–51. [CrossRef]
9. Peng, H.; Zhang, J.; Liu, Y.; Zhang, J.; Peng, Z.; Sun, Y. MR damper's modeling based on improved dual-sigmoid model. *Vib. Shock* **2019**, *38*, 216–222. [CrossRef]
10. Sharma, S. Vibration control in quarter-car model with magnetorheological (MR) dampers using Bingham model. *J. Appl. Mech. Eng.* **2018**, *7*, 1000299. [CrossRef]
11. Abdelhamed, M.; Ata, W.; Salem, A.; Khafagy, A. Effect of modified bouc-wen model parameters on the dynamic hysteresis of magnetorheological dampers. In Proceedings of the The 19th International Conference on Applied Mechanics and Mechanical Engineering, Cairo, Egypt, 7–9 April 2020; pp. 1–13.
12. Floreán-Aquino, K.H.; Arias-Montiel, M.; Linares-Flores, J.; Mendoza-Larios, J.G.; Cabrera-Amado, Á. Modern semi-active control schemes for a suspension with MR actuator for vibration attenuation. *Actuators* **2021**, *10*, 22. [CrossRef]
13. Guo, Y.-Q.; Li, M.; Yang, Y.; Xu, Z.-D.; Xie, W.-H. A Particle-Swarm-Optimization-Algorithm-Improved Jiles–Atherton Model for Magnetorheological Dampers Considering Magnetic Hysteresis Characteristics. *Information* **2024**, *15*, 101. [CrossRef]
14. Hu, H.; Hu, M.; Chen, Y.; Tang, Y. Parameter identification method of hyperbolic tangent model of magnetorheological damper. *Ship Eng.* **2017**, *39*, 31–34+75.
15. Dutta, S.; Choi, S.-B. A nonlinear kinematic and dynamic modeling of Macpherson suspension systems with a magneto-rheological damper. *Smart Mater. Struct.* **2016**, *25*, 035003. [CrossRef]
16. Chen, X.; Wu, L.; Yin, J.; Li, J.; Luo, J. Robust H∞ control design of an electromagnetic actuated active suspension considering the structure non-linearity. *Proc. Inst. Mech. Eng. Part D J. Automob. Eng.* **2019**, *233*, 1008–1022. [CrossRef]
17. Cheng, W.J.; Ren, H. Nonlinear Optimal Sliding Mode Fuzzy Control for In-Wheel Active Vibration Damper of Electric Wheel. *Automot. Eng.* **2018**, *40*, 719–725. [CrossRef]
18. Xu, M.; Huang, Q.; Li, G. Switch-optimal Control of Vehicle's Magnetorheological Semi-active Suspensions. *Noise Vib. Control* **2020**, *40*, 159–164. [CrossRef]
19. Jia, T.; Pan, Y.; Liang, H.; Lam, H.-K. Event-based adaptive fixed-time fuzzy control for active vehicle suspension systems with time-varying displacement constraint. *IEEE Trans. Fuzzy Syst.* **2021**, *30*, 2813–2821. [CrossRef]

20. Nguyen, D.N.; Nguyen, T.A. Proposing an original control algorithm for the active suspension system to improve vehicle vibration: Adaptive fuzzy sliding mode proportional-integral-derivative tuned by the fuzzy (AFSPIDF). *Heliyon* **2023**, *9*, e14210. [CrossRef]
21. Lixia, Z.; Ningfei, L.; Kuangqun, L. Research on Smooth Skyhook Control Strategy of Semi-active Suspension with Continuously Adjustable Damping. *Noise Vib. Control* **2023**, *43*, 169–173, 184.
22. Gao, J.; Li, H.; Yang, X. Research on PID-LQR Control of 7 DOF Semi-active Suspension Model. *Veh. Power Technol.* **2023**, *171*, 1–6, 23. [CrossRef]
23. Ahn, D.-V.; Kim, K.; Oh, J.; Seo, J.; Lee, J.W.; Park, Y.-J. Optimal Control of Semi-Active Suspension for Agricultural Tractors Using Linear Quadratic Gaussian Control. *Sensors* **2023**, *23*, 6474. [CrossRef] [PubMed]
24. Shao, S.; Hu, G.; Gu, R.; Yang, C.; Tu, Y. Research on GA-LQR of Automotive Semi-active Suspension Based on MRD. *Mod. Manuf. Eng.* **2021**, *11*, 9.
25. Li, G.; Gu, R.; Xu, R.; Hu, G.; Ouyang, N. Study on Fuzzy LQG Control Strategy for Semi-active Vehicle Suspensions with Magnetorheological Dampers. *Noise Vib. Control* **2021**, *41*, 129–136. [CrossRef]
26. Xiong, X.; Chen, J.; Wei, J. Research on Genetic Algorithm Optimization of LQR Control Strategy for Active Suspension. *J. Yancheng Inst. Technol.* **2024**, *37*, 60–66.
27. Sun, T.; Xu, G.; Chai, L. A Study on the Road Model with Four-wheel Non-stationary Random Excitations. *Automot. Eng.* **2013**, *35*, 868–872. [CrossRef]
28. Peng, C.; Zheng, L.; Li, Y. Optimum design of Active Suspension Actuator using Multi-objective Stochastic Particle Swarm Optimization. *J. Cent. South Univ.* **2017**, *48*, 968–997. [CrossRef]

Disclaimer/Publisher's Note: The statements, opinions and data contained in all publications are solely those of the individual author(s) and contributor(s) and not of MDPI and/or the editor(s). MDPI and/or the editor(s) disclaim responsibility for any injury to people or property resulting from any ideas, methods, instructions or products referred to in the content.